Deep water focused breaking wave loads on a fixed cylinder

Marc Batlle Martin, Jeffrey Harris, Jean-François Filipot, Florian Hulin, Alan Tassin, Paul Renaud

Deep water focused breaking wave loads on a fixed cylinder

Marc Batlle Martin[a,b], Jeffrey C. Harris[b], Jean-François Filipot[a], Florian Hulin[a,c,d], Alan Tassin[c] and Paul Renaud[a,d]

[a]France Energies Marines, Plouzané, France
[b]LHSV, Ecole des Ponts, EDF R&D, Chatou, France
[c]Ifremer, RDT, F-29280 Plouzané, France
[d]ENSTA Bretagne, UMR CNRS 6027, IRDL, 29806 Brest Cedex 09, France

ARTICLE INFO

Keywords:
Breaking waves
Slamming
Computational fluid dynamics
Floating offshore wind turbines

ABSTRACT

This paper presents new results regarding numerical simulations of breaking wave impacts on a surface-piercing cylinder. The computational fluid dynamics solver, code_saturne, using the volume of fluid approach, is presented and used for offshore hydrodynamics. Phase-focused waves are generated to recreate singular breaking events under relatively controlled conditions. The numerical results compare favorably with a recent experimental campaign for the same conditions, although there is better agreement over the force impulse than the maximum force. The fluid shape and kinematics are described during the breaking process and the load produced by a plunging breaker on a rigid cylinder is investigated.

1. Introduction

Bottom-fixed and floating offshore wind turbines are now seen as a pillar of the green energy production at global scale, being an economically viable alternative to conventional carbon-based energy forms. During the past few decades, most offshore wind turbines were installed on bottom-fixed foundations relatively close to the coastline. More recently, the energy sector is gradually embracing the possibility of expanding towards deeper waters, mostly motivated by the presence of stronger and more stable winds, and the availability of a wider range of areas. The water depths on these locations make the installation of conventional bottom fixed structures difficult, and newer approaches using floating turbines are more viable solutions.

The rapid growth of this sector and the large number of turbines to be installed in a single farm requires different approaches for their design, manufacturing, and installation, compared to the typical procedure for existing offshore structures, e.g., oil and gas. Compare to oil and gas, the offshore wind sector cannot afford over design of the systems since the financial margins generated by wind energy production are much less important. The growth of this new sector hence requires an optimization of the design methods to reduce safety factors and reach optimal design.

The targeted locations for offshore bottom fixed and floating wind turbines may be affected by impacts of energetic steep or breaking waves (ESBWs) and these may be an important contributor to the overall loading of the structure affecting the Ultimate Limit State. Unlike nonbreaking waves (e.g., Sriram et al., 2020), when ESBWs interact with offshore structures, they lead to violent motions of the liquid and a significant transfer of momentum occurs in very localised spatial and temporal scales (<0.1 s). These so-called *slamming events*, are likely to occur during storm conditions and the related resultant forces are poorly predicted if using Morison's formula (Morison et al., 1950), even with nonlinear wave kinematics or accounting for diffraction. The applicability of such an approach has been studied by Saincher et al. (2022). The waves involved in these events are very steep or breaking, and the models employed for understanding seakeeping are not designed to correctly simulate them. On the other hand, the generally accepted analytical or empirical formulations employed by engineers to predict the slamming forces are directly related to the wave shape and kinematics. These engineering formulas lead to unreliable results when fed by low fidelity hydrodynamics model. Hence, experiments or high-fidelity models (those solving the Navier-Stokes equations) are required to correctly assess slamming loads on structures. In real conditions, slamming events occur during irregular sea-state. Because the simulation of irregular sea-states is highly expensive in terms of CPU resources, focused waves are often considered as an acceptable balance between accuracy and computational costs. In a focused wave packet, dispersion of deep-water waves is used to generate one or several breaking waves embedded in wave packets through a process that is easily repeatable. Depending on the application, the spectra used to generate the wave packet can take different forms (e.g., Saincher et al., 2022), including the generation of a realistic waveform using NewWave theory, as described by Tromans et al. (1991). In modeling applications, it is important to validate the propagation even prior to breaking, as Vyzikas et al. (2021) found that different models can give moderately different results for certain harmonics of a wave group, likely due to the large steepness. Focused waves for floating structures have previously been used for blind comparative studies as a result, using NewWave theory, as described by Ransley et al. (2020).

ORCID(s): 0000-0003-0806-8192 (M. Batlle Martin); 0000-0002-8167-7974 (J.C. Harris)

The application of focused waves, at least close to the start of wave breaking, also avoids the additional questions of turbulence. Notably, for cases where the wave breaks significantly before the cylinder position, turbulence can be important (Li and Fuhrman, 2022). When it comes to validation of a numerical model, this physical distinction is important, as the choice of turbulence model can be significant when studying impact forces, as shown by Qu et al. (2021), even before considering that multiple slamming events in regular or random sea states can result in residual turbulence, air entrainement, or other physics that may affect the physics of the flow (Tomaselli and Christensen, 2017). Also, recent work by Larsen and Fuhrman (2018) also showed that many two-equation Reynolds-averaged models require stabilization to be applied to water wave problems where regions of near-potential flow exist. As our primary interest here is understanding just singular slamming events, we limit our attention to conditions where no turbulence model appears to be required, avoiding these complications, and leave more complex interactions for future work.

The original works of von Karman (1929) and Wagner (1932) represent the foundations of the slamming theory. They investigated the water entry of a rigid object on a flat surface fluid, mimicking the impact pressures on seaplanes during landing. The theory of Wagner included the pile-up effect and the full effect of the added mass as an extension to the work of von Kármán. Goda et al. (1966) extended this work for water waves, introducing the concept of the curling factor, $\lambda \in [0, 1]$, which indicates how much of the wave crest is involved in the slamming impact. A generic form of the slamming formula may be represented, following a similar notation as the one presented in Paulsen et al. (2019), as

$$F_s(z', y', t) = \frac{1}{2}\rho V^2 \cdot C_s \cdot f(t) \cdot \lambda\eta_b \cdot D \cdot g(z', y'). \quad (1)$$

where ρ is the fluid density, V is the fluid impact velocity, $C_s = 2\pi$ is the slamming coefficient for a circular cylinder entering a flat free surface according to Wagner (1932); Wienke and Oumeraci (2005). The temporal development of the force is represented by the function $f(t)$, $\lambda\eta_b$ is the portion of the wave elevation involved in the slamming impact, D is the cylinder diameter and $g(z', y')$ is a non-dimensional function taking into account the spatial distribution of the load, and may be related to the incoming wave velocity field, as discussed in Renaud et al. (2023a). In recent years, Wienke and Oumeraci (2005) further investigated experimentally the slamming load exerted by phase-focused breaking waves on an inclined slender cylinder. During the JIP-WiFi project (Paulsen et al., 2019), these existing formulas were revisited based on empirical fitting over a large number of slamming impacts produced by multiple irregular sea-states related to shallow to intermediate water depths. The particular interest in further CFD results here are to improve engineering models, however, as even for a fixed structure, Veic and Suilisz (2018) notably found that the Wienke's model (Wienke and Oumeraci, 2005), often cited, such as by the IEC design standard may not predict the forces accurately in some situations. Very recently, in the frame of the DIMPACT (Design of floating wind turbines and impacts of energetic steep and breaking waves) project, Renaud et al. (2023a) and Renaud et al. (2023b) provides enhanced slamming formulations embracing more physical process and the specificities of wave impacts on moving and tilted floating wind turbines.

The work presented in the paper is also part of the DIMPACT project which benefits from the previous experience acquired during the DiMe project (Filipot et al., 2019). DIMPACT's objectives are to reduce the uncertainties related to slamming loads exerted by ESBW on floating offshore wind turbines by analysing experimentally and numerically this phenomenon and providing ad-hoc engineering methods to address this challenge. More specifically, the objectives for this work package are to detect and evaluate the strength and weaknesses of a two phase Navier-Stokes solver, here code_saturne, to simulate phase-focused wave and the slamming loads associated on a fixed cylinder. Coherently, the objectives are extended to study phenomena linked to laboratory slamming loads which are not easily accessible experimentally, such as the pressure space-time distribution, the effect of different cylinder diameters and the comparison of undisturbed and disturbed wave characteristics during a wave impact.

The present work analyses the numerical results obtained of slamming phase-focused waves on a fixed cylinder. It intends to explore the ability of a CFD solver in capturing the impact physics with direct experimental comparisons (section 5). In section 6, different aspects of the slamming loads are explored numerically, including the pressure field space-time distributions, the effect of the breaking distance and cylinder diameter on the load magnitude. Finally, it examines the relation between the incoming wave properties and the load magnitudes.

2. Experimental setup

An experimental campaign has been carried out as part of the DIMPACT project at the Ifremer sea water wave flume in Plouzané, France. The facility is equipped with a segmented piston-type mechanism for wave generation (though for these tests all segments moved together) and an absorbing beach to limit wave reflection is used for all tests. The flume is 40.5 m long, $h = 2$ m deep at the wave generator, and 4 m wide. The flume bottom presents a slope of $-0.5\,\%$ in the longitudinal and transversal directions (water depth increases towards the beach). Four wave gauges located WG = 10.099, 10.704, 11.302, and 11.895 m upstream of the mockup are used to measure the free-surface elevation and two high-speed video cameras are used to follow the free-surface evolution at the wave breaking region.

A spar-type structure is located halfway between the wavemaker and the beach. The mockup consists in a segmented cylinder which is 1.8 m high and whose diameter is 40 cm. It is fixed to a hanging frame through an hexapod which allows precise control of the position and motion

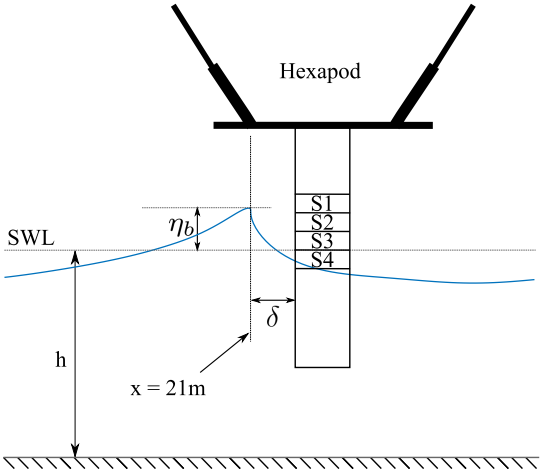

Figure 1: Sketch of the experimental model, including a mean depth h, with the locations of sections S1, S2, S3, and S4 noted. Note that horizontal locations δ are referenced as distance past 21 m, the target location of wave breaking.

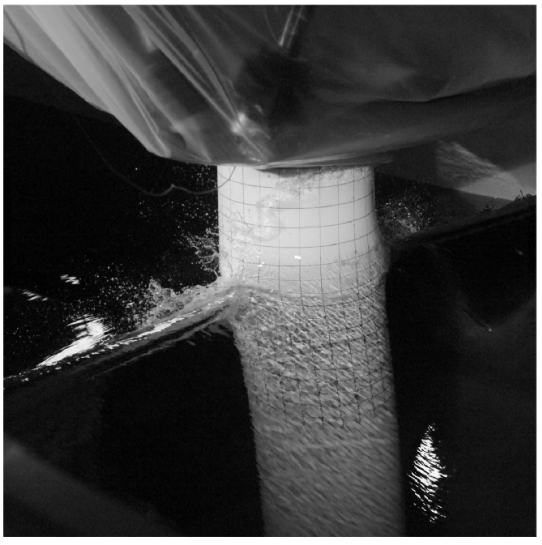

Figure 2: Typical wave impact during the experimental campaign.

(Fig. 1). The truncated cylinder is made out of six different segments, where four of them (S1 to S4) are instrumented with independent load cells which are attached to the structure through an internal backbone. A typical wave impact is shown in Fig. 2. Further details about the experimental campaign can be found in Hulin et al. (2022).

3. Numerical model

The solver employed for the present work is part of the open-source code_saturne model (Archambeau et al., 2004) developed by EDF R&D. This is a Navier-Stokes model which is able to resolve free-surface motion with multiple approaches, including a moving mesh (arbitrary Lagrangian-Eulerian or ALE) scheme (Ferrand and Harris, 2021). For the present application, in order to be able to capture the dynamics of a breaking wave, the volume of fluid (VOF) approach is used. Specifically, this is based on a version of the M-CICSAM advection scheme (Zhang et al., 2014) for algebraic VOF.

The incompressible Navier-Stokes equations are used to describe viscous fluid dynamics. For a fluid without other external forces than gravity, the equation for continuity and momentum can be written as:

$$\begin{aligned} \partial_t(\rho\overline{u}) + \nabla\cdot\left(\overline{u}\otimes\rho\overline{u}\right) &= -\nabla p + \nabla\cdot\underline{\tau}(\overline{u}) + (\rho-\rho_{void})\overline{g}\,, \\ \nabla\cdot\overline{u} &= 0\,, \\ \partial_t\alpha + \nabla\cdot(\alpha\overline{u}) &= 0\,, \end{aligned}$$

with ρ the fluid density, $\overline{u}$ the velocity, p the pressure and $\underline{\tau}$ the stress tensor. No turbulence model is used in the present work as it is assumed to be negligible for the propagation and the initial instants of the wave overturning and impact. All the conclusions drawn from the present work are obtained through the analysis of the so-called first-loading cycle or slamming load, and this occurs fast enough after the wave breaking onset to assume that the breaking-induced turbulence has not initiated for the cases here considered. Slamming loads where the breaking-induced turbulence has initiated should consider a correct turbulence modelling closure as it is presented in Li and Fuhrman (2022). The scalar field α is used in the VOF method, defined as the volume fraction of one of the two phases. In what follows, these two phases will be air and water. The air fraction (or void fraction) is:

$$\alpha = \frac{\text{air volume in a cell}}{\text{volume of the cell}}$$

The fluid properties for a cell are therefore a linear combination of the density and viscosity of air, as a function of α (i.e., $\rho = \rho_{air}\alpha + \rho_{water}(1-\alpha)$).

3.1. Wave generation

Waves are generated at the boundary by imposing the velocity field, with a zero-gradient normal to the face boundary for the VOF field (α). As an approximation, the velocity in the air phase is taken to be zero. For the water phase, the velocity field is extracted from simulations using the fully non-linear potential flow (FNPF) solver of Grilli et al. (1989); Grilli and Subramanya (1996), based on the boundary element method (BEM). A major advantage of this method is the consideration of the non-linearities caused by the piston displacement, which are taken into account by the BEM solver. The Navier-Stokes inlet boundary condition is therefore 2 m away from the wavemaker. Other wave generation methods are available such as: direct calculation and imposition of the wave kinematics together with the VOF field (Higuera et al., 2013), the relaxation zone technique (Jacobsen et al., 2012), the results from another model for important events, similar to the database of fully nonlinear wave kinematics produced by Pierella et al. (2021), or directly a coupled model could be used, such as by Corte and Grilli (2006).

The present work makes use of phase-focused waves to simulate a chosen ESBW that could represent an extreme wave within an irregular sea state. The wave packets are generated with a superposition of N sinusoidal components according to the linear wave theory, following (Rapp and Melville, 1990):

$$\eta(x,t) = \sum_{n=1}^{N} a_n cos\left[2\pi f_n(t-t_f) + k_n(x-x_f)\right]. \quad (2)$$

where a_n is the amplitude of the components and, f_n and k_n are respectively the frequency and the wave number which satisfy the linear dispersion relation. In the present work, different truncated JONSWAP spectra with a maximum frequency of 0.8 Hz, define the generated wave amplitudes. The spectra is split uniformly into 80 components, using a frequency discretisation of 0.01 Hz. The significant wave height, H_s, is an input parameter to define the spectrum before truncation. The terms x_f and t_f are the predefined linear theory estimates of the location and time of the focal point respectively. The focusing time is defined as t_f =30 s for all the configurations. Due to nonlinear interaction of the different travelling wave components, the breaking location is different than the focusing location based on the linear theory. Consequently, an iterative process using the FNPF solver is carried out to obtain the breaking location at x=21 m, see Hulin et al. (2022) for more details. The full set of test conditions are shown in Table 1.

3.2. Wave absorption

In order to absorb incoming waves and prevent reflections, a relaxation zone is implemented at the far end of the tank (Fig. 3), reducing the required computational domain length and, thus, the computational cost of the simulations. The relaxation zone method (Jacobsen et al., 2012) makes use of a region in the domain to gently force field variables to the target values φ_{target}, in this case for both the velocities and VOF field.

In the present case for the absorption region, the target velocity is zero and elevation is simply the still water level for the VOF field. After each timestep is completed, the velocity field and α are modified by applying the transformation:

$$\varphi(\overline{x},t) = \gamma_R(x)\varphi_{computed}(\overline{x},t) + (1-\gamma_R(x))\varphi_{target}(\overline{x},t), \quad (3)$$

where the weight field, γ_R, is set equal to:

$$\gamma_R = 1 - \frac{\exp(\chi_R^{3.5}) - 1}{\exp(1) - 1} \quad (4)$$

so that it varies smoothly from 0 to 1 along the length of the zone. The coordinate $\chi_R \in [0,1]$ is simply the nondimensional distance inside the relaxation zone. The result of this relaxation zone is that the target solution will be fully imposed at the boundaries when $\gamma_R = 0$ on the far boundary.

4. Numerical setup

The numerical wave tank employed for the present work is depicted in Fig. 3. It is 29 m long (from $x = 2$ m to $x = 31$ m), 1.5 m wide, and 3.2 m high, with a −0.5 % longitudinal slope increasing the domain height far from the wavemaker. To reduce the computational costs of these 3D simulations, only part of the longitudinal length of the flume and half of the domain in the transverse direction are modeled. The latter point is possible because the wave propagation and the first instants of the overturning are assumed to be two-dimensional, thus, a symmetry plane is selected as a boundary conditions for the central longitudinal section and the parallel lateral boundary. Then, half of the flume width is reduced from 2 m to 1.5 m; preliminary tests showed no significant effect but again improved computational time. The other boundary conditions are defined as: a smooth wall for the mockup, an inlet boundary for the wavemaker (see Section 3.1), a smooth wall for the bottom boundary, an open boundary for the top plane defining the velocity gradient normal to the boundary as zero and an imposed value for the air fraction of 1. And the outlet is defined as a symmetry plane with little effect on the domain as it is proceeded by the relaxation zone, see sub-sec. 3.2, which also permitted the reduction of the domains length. The absorbing zone described above is 5 m long, starting at $x = 26$ m until the end of the tank.

The computational domain is discretized into a multi-block structured non-conformal grid. The mesh is rectilinear nearly everywhere, except for the blocks directly surrounding the cylinder, where a body-fitted mesh is used. Nevertheless, non-orthogonalities are unavoidable along the boundaries of different refinement layers. Horizontally, three main regions are defined along the flume related to different wave stages, such as: the propagation, overturning and absorption. The same discretization is employed on the propagation and absorption regions, where cells have an aspect ratio of $2 = \Delta x/\Delta z = \Delta y/\Delta z$ (Δz being the cell height), suitable for resolving the curved free-surface interface. These two regions have different zones of refinements in the vertical direction, with each transition increasing the resolution by a factor of two in all three directions. The finest region corresponds to the free-surface location and has typical cell heights of $15<H_B/\Delta z<20$, whereas the regions farthest from the free-surface are four times coarser in all directions. On the overturning region, the cell height on the free-surface block is maintained but a cubic cell aspect ratio is used, $\Delta x = \Delta z = \Delta y$, allowing a better resolution of a strongly curved free-surface. Close to the cylinder, a further refinement of a factor two in all directions is applied and the finest grid region is presented over the impact region where the slamming is most likely to occur. Here the cell height is $30 < H_B/\Delta z < 40$. In radial direction from the cylinder, cells are stretched by 0.996 (i.e., the cell size in the radial direction is very slightly smaller for cells closer to the cylinder, with a difference of less than 1% between one cell and the next) to keep an approximate cell aspect ratio of $\Delta x \approx \Delta y$ and a cell length of $R/\Delta x \approx 62$ close to the cylinder boundary. For all

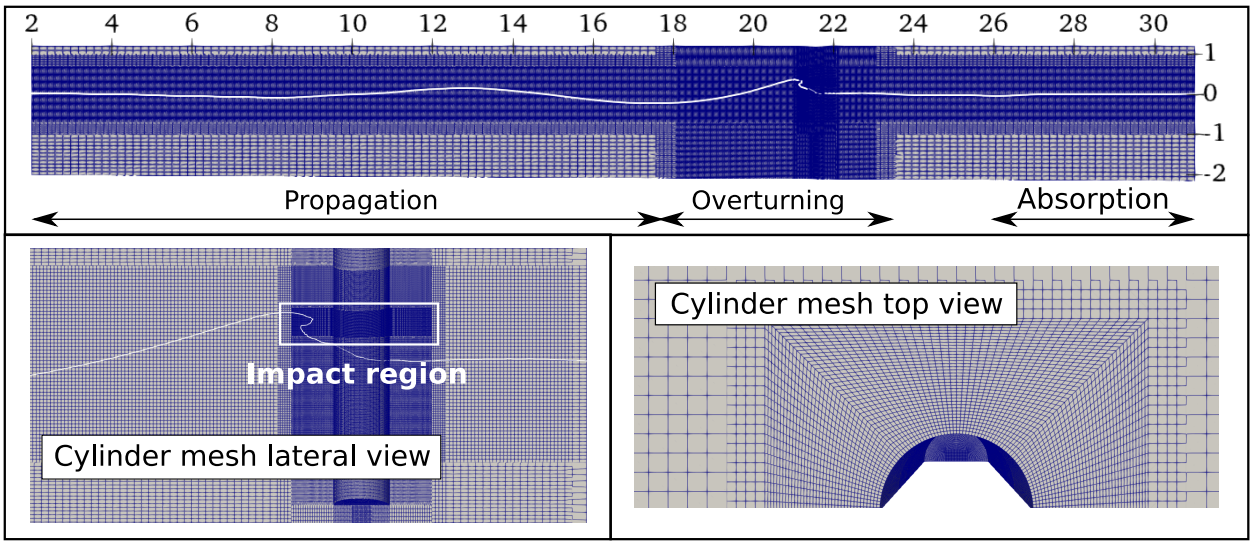

Figure 3: Detail of the 3D mesh.

the simulations presented in this work, two fixed timesteps have been used respectively for the propagation and the overturning phase. During the propagation phase, which corresponds to the time interval when the main wave remains inside the previously introduced propagation region, a time step of $\Delta t = 0.001$ s is selected. With this timestep, the propagation region horizontal cell size (free surface refinement) $\Delta x = 0.05$ m and an average value of the wave phase speed at breaking of $c = 2.5$ m/s, an indicative Courant number of $Co = (c \cdot \Delta x)/\Delta t = 0.05$ is obtained. During the overturning phase, the time step is reduced to Δt =0.000 125 s and the horizontal cell size is Δx = 0.025 m, thus, the Courant number is Co = 0.0125. These Courant numbers are seen as sufficiently small to correctly model the wave kinematics, as large Courant numbers may be a cause of early breaking, see Li and Fuhrman (2022).

Table 1 presents the test matrix for all waves conditions and different locations of the cylinder δ are presented hereafter. The water depth is the same for all the configurations and two selected peak periods locate the different test conditions within the intermediate water depths close to deep water conditions, intended to be of interest for floating offshore studies. Also, different significant wave heights, leading to different breaking strengths, are tested. The parameter δ is the distance between the cylinder front face and the target breaking location of 21 m.

5. Validation

Before proceeding into the analysis of the numerical results, the objective of this section is to quantify the accuracy and weaknesses of the hereafter presented simulations. The results for two wave configurations are compared against experimental data which is taken as a reference. First the undisturbed wave elevation evolution at four locations and the free-surface shape during the overturning is presented.

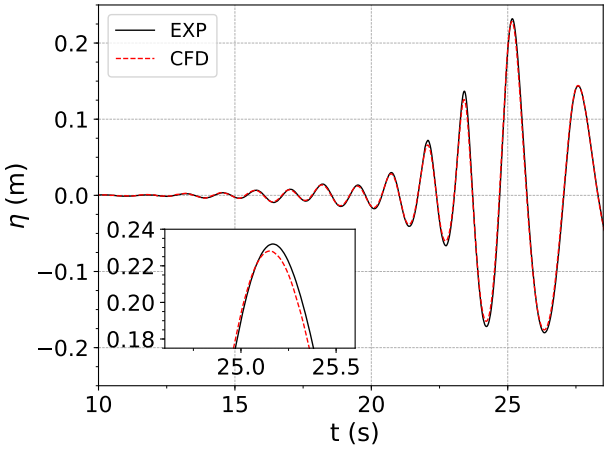

Figure 4: Free-surface evolution at different locations for H_s = 0.13 m, T_p = 2.49 s.

Next, the loads exerted by these two waves on the structure are analyzed.

5.1. Wave propagation

This section presents the free-surface elevation for two wave configurations at a given longitudinal position WG = 11.895 m, upstream of the mockup. The wave at this location is not affected by the presence of the cylinder. The numerical results are compared to the experimental wave elevation, which is obtained using a servo-controlled wave gauge (Ohana and Bourdier, 2014). The numerical results in Fig. 4 and 5 are in good agreement with the recorded experimental signals. Nevertheless, small differences are observed in the order of 0.02 s of time shift and 5 mm of free surface elevation for the focusing wave, where the CFD wave appears to be in advance and with a lower amplitude.

Table 1
Test conditions from the DIMPACT experiments.

H_s (m)	T_p (s)	γ	t_f (s)	x_f (m)	$k_p h$	δ (m)	h (m)
0.12	2.25	3.3	30	18.80	1.7	-0.2, 0.26	2
0.13	2.25	3.3	30	22.99	1.7	-0.2	2
0.15	2.25	3.3	30	24.15	1.7	-0.2, 0.16, 0.36, 0.46	2
0.17	2.25	3.3	30	27.90	1.7	-0.2	2
0.2	2.25	3.3	30	27.42	1.7	-0.2, 0.26	2
0.12	2.49	1.4	30	18.84	1.45	-0.2	2
0.13	2.49	1.4	30	19.69	1.45	-0.2, 0.36	2
0.14	2.49	1.4	30	23.42	1.45	-0.2	2
0.15	2.49	1.4	30	23.92	1.45	-0.2, 0.3	2
0.16	2.49	1.4	30	24.08	1.45	-0.2, 0.36	2
0.18	2.49	1.4	30	23.72	1.45	0.36	2

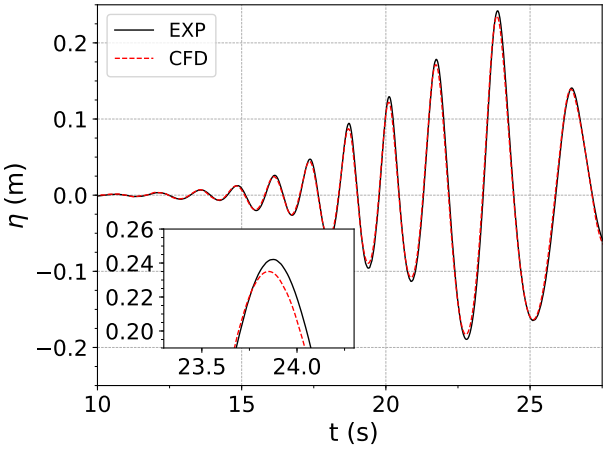

Figure 5: Free-surface evolution at different locations for H_s = 0.15 m, T_p = 2.49 s.

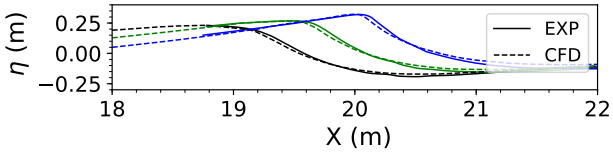

Figure 6: Free-surface profile at t=29.4, 29.6 and 29.8 s for H_s = 0.13 m, T_p = 2.49 s.

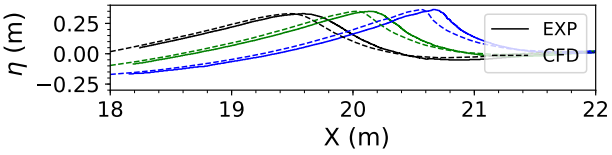

Figure 7: Free-surface profile at t=26.2, 26.4 and 26.6 s for H_s = 0.15 m, T_p = 2.49 s.

5.2. Wave shape

Fig. 6 and 7 present the undisturbed free-surface profile at three different instants of two wave overturning events. The wave is assumed to be undisturbed as the free-surface is extracted far from the central transverse section numerically, and it is extracted at the wall without the structure experimentally. An overall good agreement is observed for both configurations. Only small discrepancies are observed, the wave amplitude is fairly well conserved and small differences in the order of 5 mm are observed, similarly to what was presented for the wave elevation over time. However these differences could be expected to be more significant the larger the distance from the wavemaker. A possible explanation for this is the fact that the free-surface in this section is extracted at the flume wall where a slight friction could cause a reduction of the wave energy compared to the central flume section. On the other hand, the CFD wave is now delayed ≈ 5-10 cm on the wave crest horizontal position or 0.5 % difference of the wave celerity. This is the opposite to what was observed on the wave probes and might be related to the energy loss due to numerical diffusion, or the wave crossing through different mesh refinement regions.

5.3. Wave load

Fig. 8 and 9 presents the total horizontal force on the four cylinder sections (left) and the force for each section (right). The numerical results during the slamming event are compared with the unfiltered and filtered experimental results using a low-pass cutoff frequency of 300 Hz. Overall a fair agreement is observed between the numerical results and experiments, especially when the so called quasi-static force is the driving load contributor. This can be seen for the lowest sections, S_3 and S_4, where the cylinder is fully immersed. Nevertheless, a structural response signature is observed experimentally with two distinct frequency ranges, and this is not visible numerically as the cylinder is fixed and fully rigid. The time shift and wave profile differences observed in the previous sections are also seen in the load evolution here, with similar shifts in time and slightly different growth rates of the quasi-static force.

The most visible differences are observed on the slamming load contribution, see S_1 and S_2, with typical differences of the total maximum force magnitude compared to the filtered in the order of 30 % and 60 % for the unfiltered signal. The filtering methodology has a great influence on the experimental results, especially on the slamming contribution,

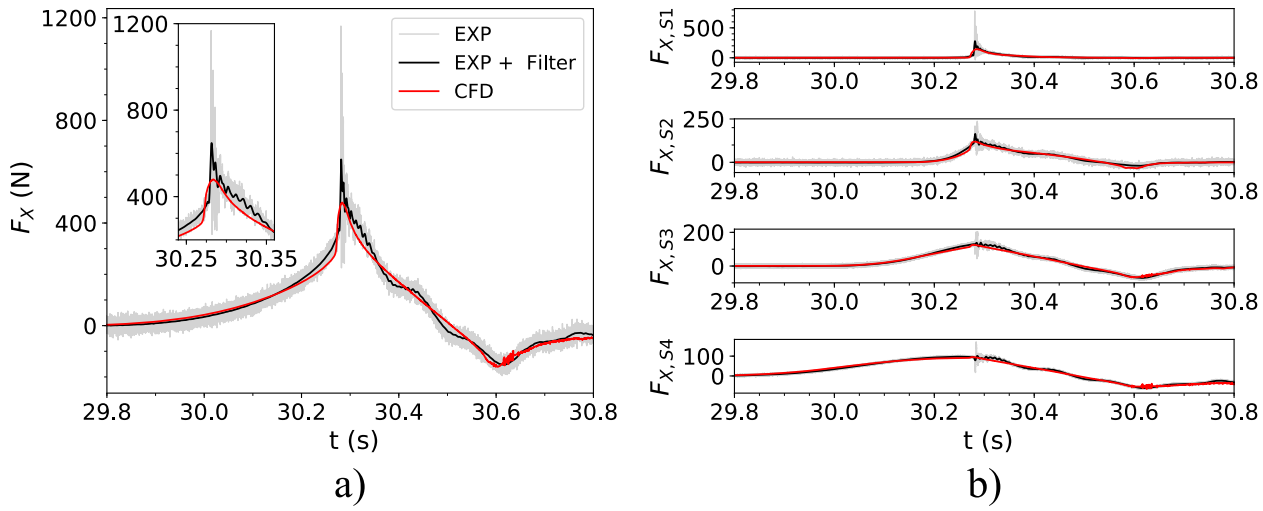

Figure 8: Horizontal force on the four sections (a) and each section (b). Case $H_s = 0.13\,\text{m}$, $T_p = 2.49\,\text{s}$ and $\delta = 0.36\,\text{m}$

and a more accurate procedure is being investigated within the DIMPACT project, but this remains outside the scope of the present work. Nevertheless, a clear underestimation of the maximum load is present numerically compared to the experiments, and this is attributed to different aspects, such as a divergence in the maximum force peak when refining either the cell size close to the structure boundary or the time step during the slamming event. This divergence is attributed to different phenomena occurring during the first instant of impact such as: the rapid expansion of the wetted surface, fluid compressibility effects or air entrapment. These have been investigated by different authors, as well as during the present project, e.g., using the cylinder water entry configuration by Zhu et al. (2007); Wang et al. (2023) or the idealised wave impact on a vertical wall (Batlle Martin et al., 2021). Another important aspect which has an influence on this peak force underestimation is the numerical diffusion of the interface at the wave front tip during the overturning. This rapidly reduces the fluid density, thus, the slamming force when the impact first begins.

5.4. Force impulse

In previous section, the underestimation of the slamming peak force for two configurations was highlighted. The present section extends the perspective and attempts to resolve this difference by comparing the maximum load captured on the highest cylinder section S_1, where the force is mainly related to the slamming effect and some residual run-up loading contribution. The numerical and experimental (filtered and unfiltered) results are compared in Fig. 10a where a clear difference in the most violent cases is presented. Following the work previously mentioned Zhu et al. (2007); Batlle Martin et al. (2021), the force impulse as the time integral of the slamming force is compared, instead of using the highly sensitive peak force. For this paper, the force impulse is calculated between -0.2 s before the maximum force (when the cylinder section where the impact occurs is fully surrounded by air, thus, the force is zero) and the maximum force instant. The maximum instant is chosen for each method (i.e., impulse is calculated experimentally for 0.2 s before the maximum force recorded experimentally, and the impulse is calculated numerically for 0.2 s before the maximum force is computed numerically), to avoid complications of small timing issues between the two. Fig. 10b presents a fair correlation of the calculated numerical and experimental force impulse and serves to validate the here presented numerical model. That said, quantities like the so called rise time and the maximum force, which are physically related, are currently inaccessible numerically and need further investigation. From an engineering perspective, both the maximum force and the force impulse are valuable parameters during the design process, and recent work regarding a semi-analytical methodology to define the force impulse of a breaking wave is presented in Ghadirian and Bredmose (2019). From these sections, one may conclude that the numerical model is a reliable tool to investigate phase-focused slamming loads to a certain extent. The simulation of the experimental breaking wave is fairly well validated with some visible differences which are mainly attributed to the wave generation model. Regarding the so-called slamming component of the wave load, the magnitude and duration of the force present visible differences compared to the experimental results, whereas, a greater agreement is observed for the quasi-static loads. On the other hand, the fluid momentum represented by the force impulse is observed to be in agreement with the experiments. Coherently from these conclusions, the next sections aim to investigate reliable information such as the load spatial distribution, the influence of the cylinder on the wave flow and the relation between the wave geometry and kinematics.

6. Results

This section objectives are: to evaluate the typical pressure vertical distribution of the slamming load on the cylinder, to investigate the limitations of using an undisturbed

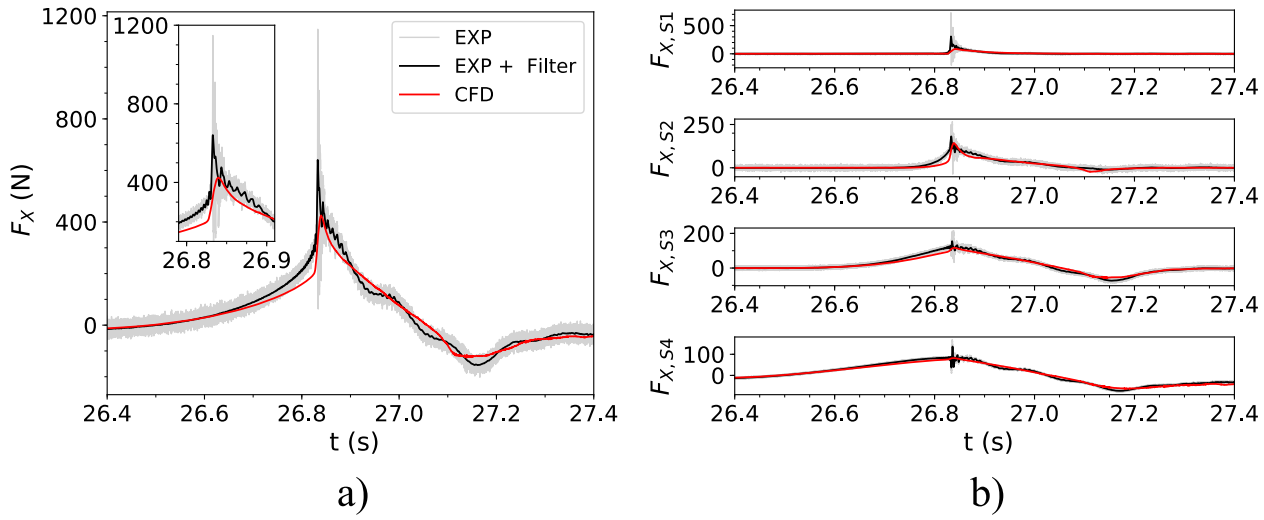

Figure 9: Horizontal force on the four sections (a) and each section (b). Case $H_s = 0.15\,\mathrm{m}$, $T_p = 2.49\,\mathrm{s}$ and $\delta = 0.3\,\mathrm{m}$.

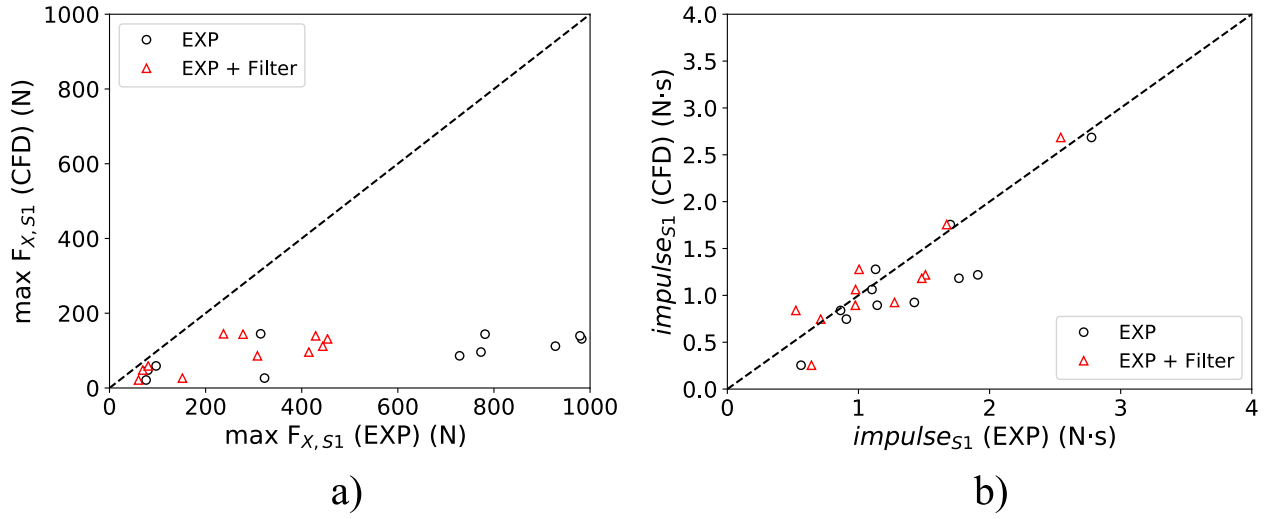

Figure 10: Comparison of the experimental and numerical maximum force (a) and the force impulse (b) at the highest section (S_1)

wave to calculate the slamming load, the disturbance of the structure on the incoming wave (e.g., run-up) and its influence on the slamming load and to evaluate the possible relation between a wave breaking strength parameter and the so-called curling factor.

6.1. Wave impact pressure distribution

One of the main reasons that motivated the present numeric study, in complement to experimental tests, is the accessibility of the dynamics and kinematics of the flow field during a slamming event. Fig. 11 presents the non-hydrostatic pressure field p_d during a slamming scenario, with the top panel showing the evolution of this field over the cylinder front face vertical axis, and the bottom panel showing four relevant instants (t = 26.716, 26.728, 26.756, 26.85 s) during the loading process in 3D. Two vertical dashed lines have been depicted in the spatio-temporal diagram defining the impulse time, which is the interval of interest and applicability of the present work. Phenomena occurring after this interval are also described in the next paragraph, but this should be regarded as approximate due to the fact that turbulence may be present during those stages and it is not modelled in the present work. Similar analysis has been carried out by other authors for shallow water conditions and wave loads on a monopile Veic et al. (2019) or on a tripod Hildebrandt et al. (2013).

From this diagram, four different stages of the slamming are identifiable, as initially (a) the first contact of the overturning wave tip meets the structure and leads to a highly localised pressure rise typically within at the breaking wave elevation or slightly below. This jet spreads upwards and downwards, the latest at the same time impacts the fluid of the lower part of the air cavity and present the two singular high pressure locations presented as (b) in the diagram. At this instant, the air that might be entrapped between the incoming wave and the cylinder escapes rapidly. For

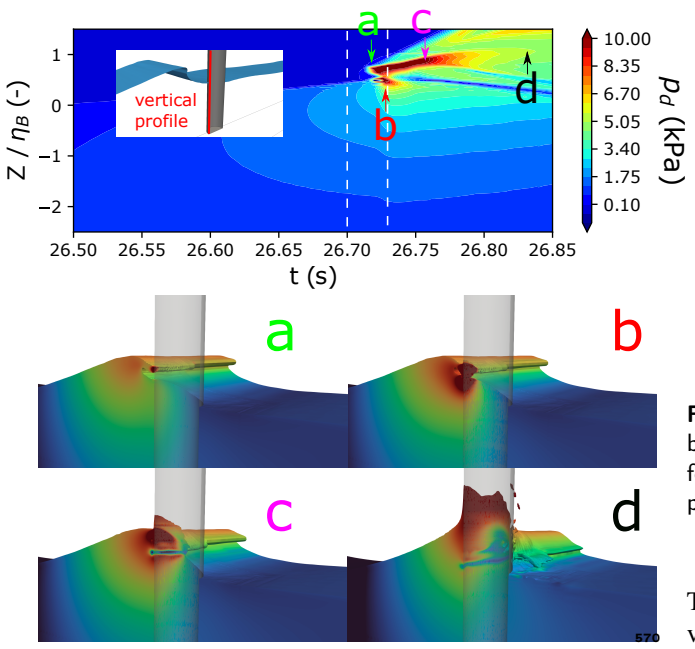

Figure 11: Spatio-temporal non-hydrostatic pressure distribution on the cylinder front face vertical axis and evolution (top) and non-hydrostatic pressure field for $\alpha < 0.5$ at four instants ($t = 26.716, 26.728, 26.756, 26.85\,\mathrm{s}$) during a slamming event for $H_s = 0.18\,\mathrm{m}$ and $T_p = 2.49\,\mathrm{s}$, with $\delta = 0.36\,\mathrm{m}$.

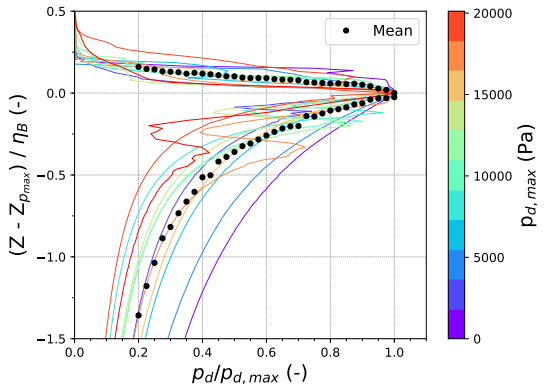

Figure 12: Normalised non-hydrostatic pressure vertical distribution on the cylinder front face vertical axis at the maximum force instant. Black dots indicate the average nondimensional pressure for a given nondimensional vertical level.

plunging breakers and small cylinder radius, the volume of air is expected to be small and the collapse of the cavity duration to be large enough not to induce air compressibility effects, but this could be considered for further analysis. For the present study, transverse velocities of air flowing out from this cavity have been observed in the range of 15 m/s and maximum gauge pressure of 20 kPa which are typically located at the water-cylinder contact, decreasing inside the air cavity.

The impossibility of the jet to avoid the obstacle flowing downwards, transfers all the momentum upwards presenting the splash loading signature on the diagram (c) and finally leading to the run-up (d). At the snapshot (c), a tubular low pressure region appears surrounding the cylinder has been attributed to the previously mentioned downwards jet, which, due to the impossibility to continue moving downwards it flows opposite to the wave propagation direction. To the best of the authors' knowledge, this phenomenon has not been observed previously and needs further investigation. It further suggests that slamming events not only cause intense vertically-integrated loads on cylindrical offshore structures such as OWT but also may cause highly localized pressure peak, hence stresses and potential damages on the structure.

Fig. 12 presents the vertical distribution of pressure on the cylinder front face vertical axis at the maximum total force instant for all the different test conditions where the wave breaking occurs in front or before the cylinder front. A similar graph, experimentally, is proposed in Paulsen et al. (2019) for irregular waves in shallow water conditions.

The color map from this graph presents that for the less violent configurations, the loading is typically more broadly distributed over the vertical and the slamming contribution is more comparable to the quasi-static load. For the more intense cases, the slamming load is more localised and has a significantly higher magnitude that the quasi-static load. For some of the configurations, the presence of an air cavity lowered the pressure magnitude over that area slightly below the pressure maxima. An average vertical pressure distribution is further calculated above and below the maximum pressure location.

In order to quantify a curling factor, one can identify the region where the normalized pressure maximum exceeds some value, with this threshold at first unknown. For the higher elevations (Fig. 12), this threshold is generally clear, but for points lower than the impact point, the pressure low inside the air cavity makes this threshold unclear, as there is again high pressure below the air cavity. For the lower curve, then, the point above the air cavity is used to calculate the mean elevation for the different pressure fractions. The vertical distances over which this threshold is satisfied can be seen as the wave elevation portion which contributes to the maximum load pressure fraction, and this has a clear resemblance to the so called curling factor, λ. If this vertical portion is calculated for each curve and presented against the pressure portion, similar to Paulsen et al. (2019), we can obtain the profiles of Fig. 13, together with the curling factor related to the mean profile.

From Fig. 13, one can extract that this analysis could be misleading for certain low intensity slamming conditions as the curling factor would be larger compared to more violent event. Nevertheless, the mean value of the curling factor obtained for the different tested conditions in the present work, has a value of approximately 0.4 for a pressure value of 50 % of the peak slamming pressure, which is the same as the one obtained in Paulsen et al. (2019).

In section 6.3, we further propose an alternative method to assess the curling factor.

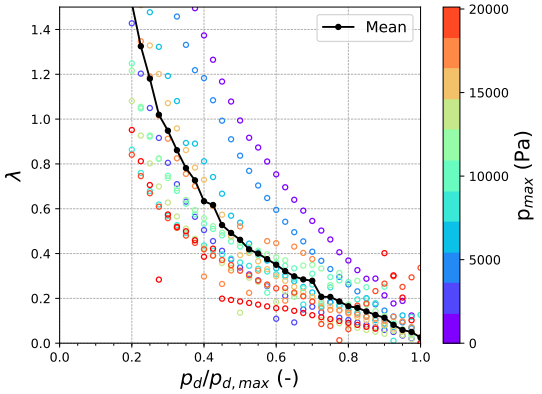

Figure 13: Wave elevation portion, or curling factor, related to the maximum non-hydrostatic pressure fraction.

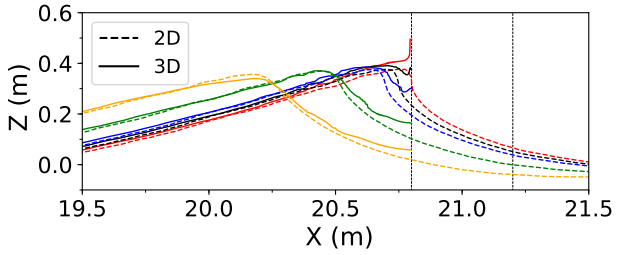

Figure 14: Undisturbed (2D) and disturbed (3D) by the cylinder free surface profile at different time instants t = 26.35,26.45, 26.52, 26.54 and 26.56 m, for H_s = 0.15 m and T_p = 2.25 s, with $\delta = -0.2$ m.

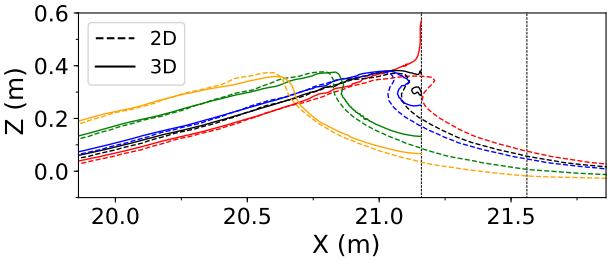

Figure 15: Undisturbed (2D) and disturbed (3D) by the cylinder free surface profile at different time instants t = 26.5, 26.7, 26.57, 26.65 and 26.67 m, for H_s = 0.15 m and T_p = 2.25 s, for H_s = 0.15 m and T_p = 2.25 s with $\delta = 0.16$ m.

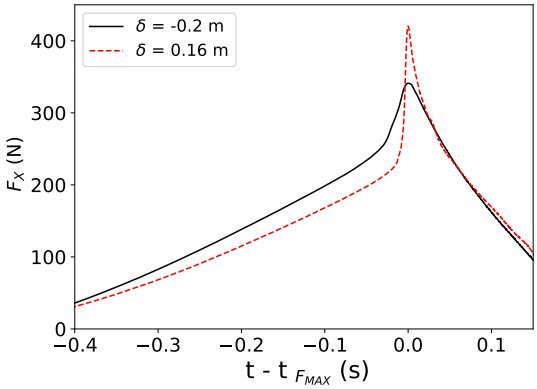

Figure 16: Total horizontal force on the cylinder for two different locations for the cylinder $\delta = -0.2$ m and 0.16 m.Case H_s = 0.15 m, T_p = 2.25 s.

6.2. Effects of the cylinder diameter and location

This section is dedicated to the effect of the structure presence on the slamming load. First, the undisturbed free surface ($\alpha = 0.5$) of the wave has been simulated in 2D without any obstacle and it has been compared to the free surface at the central longitudinal section affected by the cylinder, see Fig. 14 and 15. For the same wave, the cylinder has been located at two different distances from the expected breaking location of $x = 21$ m. In Fig. 14, which corresponds to $\delta = -0.2$ m, one can observe that the location of the wave front when it becomes vertical in 2D (red curve) is at the same location as the cylinder front face. This situation is expected to produce the maximum load, however, the presence of the cylinder induces an run-up which re-directs the wave front momentum upwards. If the cylinder is located downstream at $\delta = 0.16$ m, Fig. 15, the effect of the run-up is lowered and the overturning tip impact directly the structure. From this late scenario, it is also observable that the wave crest is slightly advanced in time compared to the undisturbed wave.

The run-up effect due to the structure presence has a great effect on the slamming load, see Fig. 16. The run-up increases the quasi-static load, reduces the maximum force magnitude and expands this over a longer interval. The configuration with $\delta = 0.16$ m, the wave overturning is in a slightly more advanced stage and the breaking-induced turbulence would gradually start being relevant. The lack of a turbulence model in the present work may imply a slight reduction of the force peak, meaning that the differences caused by the presence of the cylinder would be even larger. In this scope, this effect has been exemplified by moving the cylinder location but investigation about the direct effect of the distance between the wave breaking point and the cylinder front face are being carried in parallel and the first experimental conclusions can be found in Hulin et al. (2022). Other authors have explored this distance before, e.g., the experimental work of Zhou et al. (1991).

Fig. 17 presents the free surface evolution for different diameters of the cylinder maintaining the cylinder front face location. The cylinder diameter is scaled using L_B, the wavelength at breaking, which is obtained through the linear dispersion relation using the calculated phase speed based on the wave crest horizontal position ($c^2 = g(L_B/2\pi)\tanh(2\pi h/L_B)$). It is observed that higher diameters lead to higher run-up by reduction of the vertical portion of the wave front acting directly on the cylinder. The phase speed is also slightly influenced, increasing for the higher cylinder diameter.

Fig. 18 presents the scaled horizontal force. The total load is apparently higher for larger cylinder diameters, this is mostly a consequence of the higher quasi-static load where the inertia contribution is highly affected by the $\rho g D H_S^2$

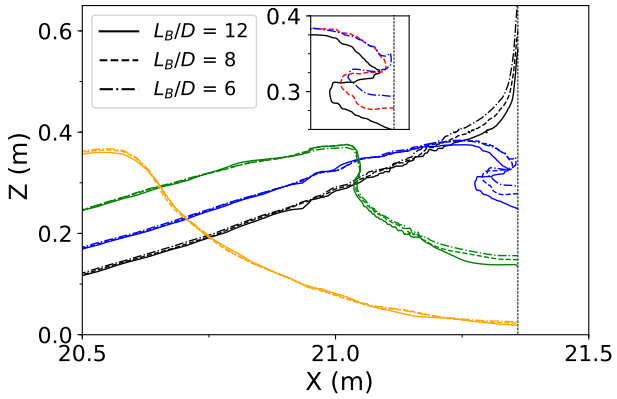

Figure 17: Free surface at four instants during a slamming for three different cylinder diameters for $H_s = 0.15\,\text{m}$ and $T_p = 2.25\,\text{s}$, with $\delta = 0.36\,\text{m}$.

scaling. Nevertheless, this scaling presents a similar slamming coefficient for the highest section S_1. The evolution is slightly different and this is attributed to the fast growth of the run-up for the two bigger diameters, as observed in Fig. 17.

6.3. Relating impact force to incoming wave

Ideally, it would be possible to approximate the impact forces without passing through such complex 3D simulations, knowing only the kinematic and geometry of the incoming wave alone, as done in engineering methods implementing semi-analytical formulas of .e.g. Goda et al. (1966). One difficulty that arises in the problem of slamming loads assessment using semi-analytical formula (see equation 1) is the definition of the curling factor λ that gives the proportion of the crest height causing slamming loads which translates the severity of the breaking waves.

Recently, Derakhti et al. (2018) proposed a parameter Γ to quantify the breaking wave severity of a crest in relation to its energy dissipation, here defined as:

$$\Gamma = T_B \frac{d(u/c)}{dt} \tag{5}$$

with $T_B = L_B/c$ is a characteristic period, u the horizontal fluid velocity at the crest and c the crest phase speed, calculated at the instant that $u/c = 0.85$. Note that this is slightly different than the definition of Γ used by Derakhti et al. (2018) due to choosing L_B from the crest velocity instead of trying to estimate the distance between zero-crossings in the wave elevation. In addition to the possibility of load models as Renaud et al. (2023a), we can consider wave crest properties such as the value of Γ that Derakhti et al. (2018) found to be important for understanding wave dissipation, to see if it also could be related to λ.

Curling factor The first challenge is to provide an unambiguous measure of the curling factor λ from a given breaking wave, which in theory corresponds to the ratio between the height of the vertical crest front and the total crest elevation. Indeed, since the crest front is only locally vertical in general, the estimation of this quantity is not achievable in practice using only geometric information. Observing the resultant horizontal force evolution on a cylinder during a slamming event, a typical signature is visible as a force growth changing from the phase speed wave scale to a much sudden rise and fall of the force. Assuming that a separation of a so-called quasi-static or non-breaking and a slamming force is possible, different approaches are imaginable and, some methods based on the force evolution, are investigated in Ghadirian et al. (2023). As a continuation, the present work makes use of the referred improved quadratic polynomial method to provide an objective measure of the *curling factor*. This assumes a smooth quasi-static load time series and the possibility to identify the instant when the slamming load cycle starts such as the inflection point or when the second derivative turns to zero. Using this instant, a quadratic polynomial is fitted by defining a second point where the parabola slope has a less than 10% relative difference with the slope of the original force time series (see Fig. 20). Using this definition, one could investigate the vertical portion of the wave which contributes to the slamming as the distance between the maximum wave elevation and the wave profile intersection point with the cylinder front face, at the slamming initiation and the undisturbed wave profile. This distance may be referred as the so-called curling factor.

Breaking severity The calculation of the breaking severity Γ for the present work is a continuation of Batlle Martin et al. (2022). The phase speed c is seen as the most challenging parameter. It is derived from the horizontal crest position temporal series. Nevertheless, this evolution is non-smooth due to the crest's relatively low curvature principally related to the orthogonal mesh disposition. To overcome this, the present work assumes a linear evolution of the crest horizontal position (constant phase speed) over small time intervals ($\Delta t < T_P/10$) and the crest region as the centroid of the 3% top wave elevation. The crest speed is calculated as the average horizontal velocity of the crest free surface, this being defined as the void fraction iso-contour of 0.5. Following the definition proposed in Derakhti et al. (2018), the breaking onset occurs when the ratio between $B = u/c$ is 0.85 and a linear fit in the interval $|B - B_{th}| < 0.03$ (being B_{th} at the onset instant) is used to calculated $d\,B_{th}/dt$. The calculation of the wave breaking period T_B, typically calculated using the breaking wave length L_{th} and the linear dispersion relation, is calculated using the phase speed and the linear dispersion relation. This method preserves the relation with the wave at breaking, without the necessity of calculating the wave length using the zero-crossing method. For certain configurations, abnormally large values of the wave length have been detected and are related to the downstream displacement of the second zero crossing due to two consecutive waves overlapping.

Fig. 19 displays estimations of Γ versus λ for several waves with different input parameters and a range of non-dimensional breaking distances to mockup (δ/L_B). Although the results are scarce and scattered, they seem to

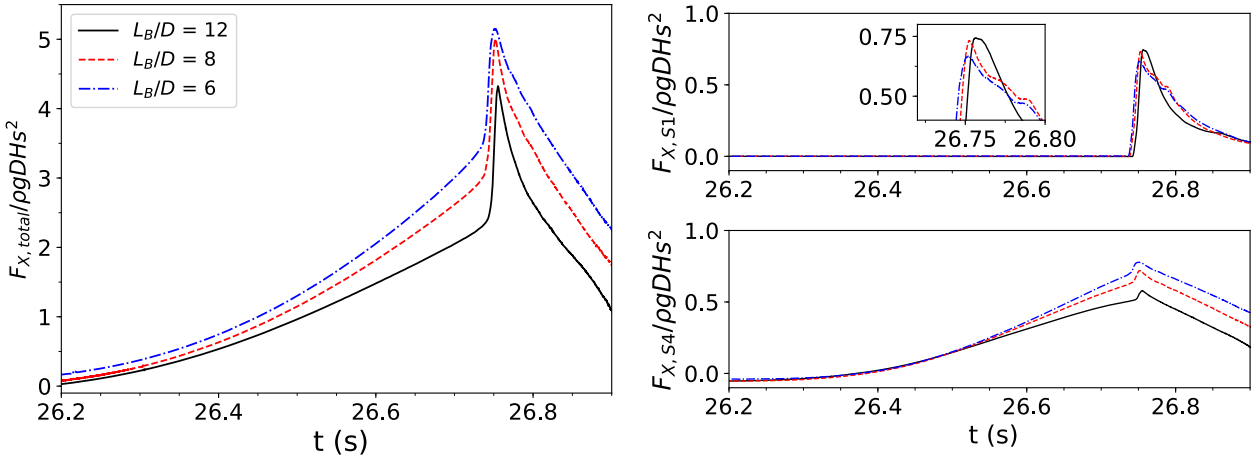

Figure 18: Total scaled horizontal load (left) and scaled horizontal load on two sections (S_1, S_4) (right) for $H_s = 0.15\,\mathrm{m}$ and $T_p = 2.25\,\mathrm{s}$, with $\delta = 0.36\,\mathrm{m}$.

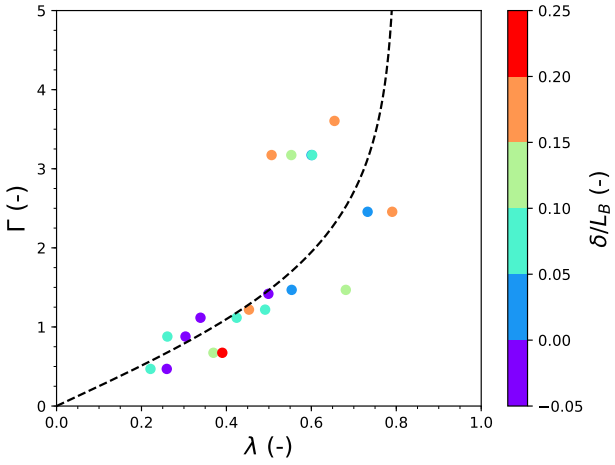

Figure 19: Relation between λ and Γ for the DIMPACT experimental cases. The color of the points indicates the non-dimensional distance between the initiation of wave breaking and the impact with the cylinder.

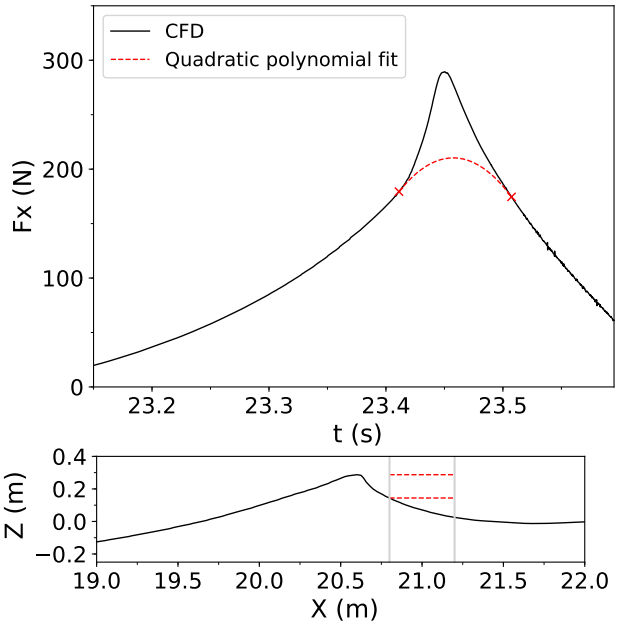

Figure 20: Demonstration of calculation of curling factor, λ, using the quadratic polynomial fit as proposed by Ghadirian et al. (2023).

be consistent with a positive correlation between Γ and λ. Although these results are preliminary, we propose here an approximate curve fit between Γ and λ (but ignoring variations with δ):

$$\lambda \approx 0.8 \tanh(0.5\Gamma) \tag{6}$$

We believe this, with further refinements to include the effect of the distance from breaking, δ, will be useful to future understand the relation between the incoming wave properties and the slamming loads intensity and refine the assessment of impact using engineering approaches. Still, an extension of the present study, covering a wider range of wave severity is required to consolidate these findings.

In particular, a wider and denser range of wave breaking severity should be covered to remove the potential bias introduced by the consideration of different nondimensional breaking point-to-cylinder distance that complicates the interpretation of the data. Indeed, a wave with a given breaking severity Γ may be associated to different curling factor depending on the stage of breaking δ/L_B. To circumvent this difficulty, further investigation should consider wave impact at a given δ/L_B and preferably at $\delta/L_B = 0$ as well.

7. Conclusion

This paper presents some of the results obtained during the DIMPACT project. The VOF solver integrated into the finite volume open-source code_saturne is used for the simulation of a numerical wave tank, investigating phase-focused waves and slamming events on a rigid cylinder. One-way coupling using the kinematic fields from a fully non-linear potential flow solver is used to generate phase-focused

waves. The ability to generate and propagate these waves is investigated through direct comparison with experimental results, first from time-series and then using the spatial distribution of the free-surface at an instant shortly before the breaking onset. An overall good agreement is presented, however, small differences in the wave amplitude and phase speed are also visible and require further investigation. The loads exerted by these waves at breaking on a fixed cylinder are compared with the experimental temporal series. The non-breaking or quasi-static wave load contributions are well captured, however, the load phenomena related to the slamming contributions are consistently underestimated. A good agreement between the numeric and experimental results is observed for the slamming load impulse.

The non-hydrostatic pressure vertical distribution on the cylinder during slamming is investigated, and a typical triangular distribution of the wave load and a double-peak vertical pressure distribution, related to the presence of an air cavity, is presented as in previous studies Paulsen et al. (2019). The methodology to determine the curling factor based on the pressure vertical distribution is analyzed and larger values of the curling factor for low-severity slamming configurations are detected. The use of the undisturbed wave shape and kinematics to calculate the slamming load is analysed by comparing the free surface modification caused by the cylinder presence and the direct impact on the slamming load. Different cylinder diameters are employed to investigate the diffraction effects on the slamming coefficient and these are observed to have little effect.

Exploratory work also shows a possible link between the curling factor to wave kinematics such as the Γ parameter of Derakhti et al. (2018). Although preliminary, there indeed seems to be a link between the two, with a more rapid breaking process being associated with a higher curling factor. In future work, we will build on these capabilities through adding results for moving and inclined cylinders, and further links to engineering models for practical use.

Acknowledgements

This work is performed under financial support of grant ANR-10-IEED-0006-34, France Energies Marines project DIMPACT (Dimensionnement d'éoliennes flottantes prenant en compte les impacts de la raideur et du déferlement des vagues).

References

Archambeau, F., Mechitoua, N., Sakiz, M., 2004. Code saturne: a finite volume code for the computation of turbulent incompressible flows - industrial applications. International Journal on Finite Volumes 1, 1–62.

Batlle Martin, M., Harris, J., Renaud, P., Hulin, F., Filipot, J., 2022. Numerical investigation of slamming loads on floating offshore wind turbines, in: International Ocean and Polar Engineering Conference, p. 6. ISOPE-I-22-031.

Batlle Martin, M., Pinon, G., Reveillon, J., Kimmoun, O., 2021. Computations of soliton impact onto a vertical wall: Comparing incompressible and compressible assumption with experimental validation. Coastal Engineering 164, 103817. doi:10.1016/j.coastaleng.2020.103817.

Corte, C., Grilli, S., 2006. Numerical modeling of extreme wave slamming on cylindrical offshore support structures, in: Proc. 16th Offshore and Polar Engng. Conf., pp. 394–401.

Derakhti, M., Banner, M.L., Kirby, J.T., 2018. Predicting the breaking strength of gravity water waves in deep and intermediate depth. Journal of Fluid Mechanics 848. doi:10.1017/jfm.2018.352.

Ferrand, M., Harris, J., 2021. Finite volume arbitrary Lagrangian-Eulerian schemes using dual meshes for ocean wave applications. Computers and Fluids 219, 104860. doi:10.1016/j.compfluid.2021.104860.

Filipot, J.F., Guimaraes, P., Leckler, F., Hortsmann, J., Carrasco, R., Leroy, E., Fady, N., Accensi, M., Prevosto, M., Duarte, R., Roeber, V., Benetazzo, A., Raoult, C., Franzetti, M., Varing, A., Le Dantec, N., 2019. La jument lighthouse: a real-scale laboratory for the study of giant waves and their loading on marine structures. Philosophical Transactions of the Royal Society A: Mathematical, Physical and Engineering Sciences 377, 20190008. doi:10.1098/rsta.2019.0008.

Ghadirian, A., Bredmose, H., 2019. Pressure impulse theory for a slamming wave on a vertical circular cylinder. Journal of Fluid Mechanics 867, R1. doi:10.1017/jfm.2019.151.

Ghadirian, A., Pierella, F., Bredmose, H., 2023. Calculation of slamming wave loads on monopiles using fully nonlinear kinematics and a pressure impulse model. Coastal Engineering 179, 104219. doi:10.1016/j.coastaleng.2022.104219.

Goda, Y., Haranaka, S., M., K., 1966. Study of impulsive breaking wave forces on piles. Technical Report. Port and Harbour Res. Inst., Ministry of Transport.

Grilli, S.T., Skourup, J., Svendsen, I.A., 1989. An efficient boundary element method for nonlinear water waves. Engineering Analysis with Boundary Elements 6, 97–107. doi:10.1016/0955-7997(89)90005-2.

Grilli, S.T., Subramanya, R., 1996. Numerical modeling of wave breaking induced by fixed or moving boundaries. Computational Mechanics 17, 374–391. doi:10.1007/BF00363981.

Higuera, P., Lara, J.L., Losada, I.J., 2013. Realistic wave generation and active wave absorption for Navier–Stokes models: Application to OpenFOAM®. Coastal Engineering 71, 102 – 118. doi:10.1016/j.coastaleng.2012.07.002.

Hildebrandt, A., Sriram, V., Schlurmann, T., 2013. Simulation of focusing waves and local line forces due to wave impacts on a tripod structure, in: Proceedings of the International Offshore and Polar Engineering Conference, pp. 575–581.

Hulin, F., Batlle Martin, M., Renaud, P., Tassin, A., Filipot, J.F., Jacques, N., 2022. Experimental investigation of the hydrodynamic loads induced by breaking wave impacts on a spar-type floating offshore wind turbine substructure , in: Proc. Journées de l'Hydrodynamique, p. 14 pp.

Jacobsen, N.G., Fuhrman, D.R., Fredsøe, J., 2012. A wave generation toolbox for the open-source cfd library: Openfoam®. International Journal for Numerical Methods in Fluids 70, 1073–1088. doi:10.1002/fld.2726.

von Karman, T., 1929. The Impact on Seaplane Floats during Landing. Technical Report. National Advisory Committee for Aeronautics Technical.

Larsen, B.E., Fuhrman, D.R., 2018. On the over-production of turbulence beneath surface waves in reynolds-averaged navier–stokes models. Journal of Fluid Mechanics 853, 419–460. doi:10.1017/jfm.2018.577.

Li, Y., Fuhrman, D.R., 2022. On the turbulence modelling of waves breaking on a vertical pile. Journal of Fluid Mechanics 953, A3. doi:10.1017/jfm.2022.941.

Morison, J., Johnson, J., Schaaf, S., 1950. The Force Exerted by Surface Waves on Piles. Journal of Petroleum Technology 2, 149–154. doi:10.2118/950149-G.

Ohana, J., Bourdier, S., 2014. Test tank related instrumentation and best practice. Technical Report. Marine Renewables Infrastructure Network (MARINET). URL: https://archimer.ifremer.fr/doc/00214/32572/31040.pdf.

Paulsen, B.T., de Sonneville, B., van der Meulen, M., Jacobsen, N.G., 2019. Probability of wave slamming and the magnitude of slamming loads on offshore wind turbine foundations. Coastal Engineering 143, 76–95. doi:10.1016/j.coastaleng.2018.10.002.

Pierella, F., Lindberg, O., Bredmose, H., Bingham, H.B., Read, R.W., Engsig-Karup, A.P., 2021. The DeRisk database: Extreme design waves for offshore wind turbines. Marine Structures 80, 103046.

Qu, S., Liu, S., Ong, M.C., 2021. An evaluation of different rans turbulence models for simulating breaking waves past a vertical cylinder. Ocean Engineering 234, 109195. doi:10.1016/j.oceaneng.2021.109195.

Ransley, E., Yan, S., Brown, S., Hann, M., Graham, D., Windt, C., Schmitt, P., Davidson, J., Ringwood, J., Musiedlak, P.H., Wang, J., Wang, J., Ma, Q., Xie, Z., Zhang, N., Zheng, X., Giorgi, G., Chen, H., Lin, Z., Qian, L., Ma, Z., Bai, W., Chen, Q., Zang, J., Ding, H., Cheng, L., Zheng, J., Gu, H., Gong, X., Liu, Z., Zhuang, Y., Wan, D., Bingham, H., Greaves, D., 2020. A blind comparative study of focused wave interactiosn with floating structures (CCP-WSI Blind Test Series 3). International Journal of Offshore and Polar Engineering 30, 1–10.

Rapp, R.J., Melville, W.K., 1990. Laboratory measurements of deep-water breaking waves. Philosophical Transactions of the Royal Society of London. Series A, Mathematical and Physical Sciences 331, 735–800.

Renaud, P., Batlle Martin, M., Scolan, Y.M., Filipot, J.F., Harris, J.C., Hulin, F., 2023a. Semi-analytical load models describing the progressive immersion of a fixed vertical cylinder in a breaking wave. Ocean Engineering 276, 114116.

Renaud, P., Hulin, F., Batlle Martin, M., Scolan, Y.M., Tassin, A., Jacques, N., Harris, J.C., Filipot, J.F., 2023b. Semi-analytical load models accounting for the tilt and motion of a cylinder impacted by a plunging breaking wave, in: Proc. 42th International Conference on Ocean, Offshore and Arctic Engineering, p. 10 pp.

Saincher, S., Sriram, V., Agarwal, S., Schlurmann, T., 2022. Experimental investigation of hydrodynamic loading induced by regular, steep non-breaking and breaking focused waves on a moving cylinder. European Journal of Mechanics - B/Fluids doi:10.1016/j.euromechflu.2021.12.009.

Sriram, V., Agarwal, S., Schlurmann, T., 2020. Laboratory study on steep wave interaction with fixed and moving cylinder, in: Proc. 30th International Ocean and Polar Engineering Conference, p. 2221.

Tomaselli, P.D., Christensen, E.D., 2017. A CFD Investigation on the Effect of the Air Entrainment in Breaking Wave Impacts on a Mono-Pile, p. V07AT06A072. doi:10.1115/OMAE2017-62445.

Tromans, P., Anaturk, A., Hagemeijer, P., 1991. A new model for the kinematics of large ocean waves-application as a design wave, in: Proc. 1st International Conference on Ocean, Offshore and Arctic Engineering, p. 15 pp.

Veic, D., Suilisz, W., 2018. Impact pressure distribution on a monopile structure excited by irregular breaking wave. Polish Maritime Research 25, 29–35.

Veic, D., Sulisz, W., Soman, R., 2019. Effect of breaking wave shape on impact load on a monopile structure. Brodogradnja 70, 25–42. doi:10.21278/brod70302.

Vyzikas, T., Stagonas, D., Maisondieu, C., Greaves, D., 2021. Intercomparison of three open-source numerical flumes for the surface dynamics of steep focused wave groups. Fluids 6, 28 pp. doi:10.3390/fluids6010009.

Wagner, H., 1932. Phenomena associated with impacts and sliding on liquid surface. ZAMM - Journal of Applied Mathematics and Mechanics / Zeitschrift für Angewandte Mathematik und Mechanik 12, 193–215. doi:10.1002/zamm.19320120402.

Wang, K., Ma, X., Bai, W., Qian, L., Li, Z., Li, Y., 2023. Two-dimensional numerical simulation of water entry of a cylinder into waves using openfoam. Ocean Engineering 269, 113516. doi:10.1016/j.oceaneng.2022.113516.

Wienke, J., Oumeraci, H., 2005. Breaking wave impact force on a vertical and inclined slender pile—theoretical and large-scale model investigations. Coastal Engineering 52, 435–462. doi:10.1016/j.coastaleng.2004.12.008.

Zhang, D., Jiang, C., Liang, D., Chen, Z., Yang, Y., Shi, Y., 2014. A refined volume-of-fluid algorithm for capturing sharp fluid interfaces on arbitrary meshes. Journal of Computational Physics 274, 709–736. doi:10.1016/j.jcp.2014.06.043.

Zhou, D., Chan, E., Melville, W., 1991. Wave impact pressures on vertical cylinders. Applied Ocean Research 13, 220–234. doi:10.1016/S0141-1187(05)80046-X.

Zhu, X., Faltinsen, O.M., Hu, C., 2007. Water Entry and Exit of a Horizontal Circular Cylinder. Journal of Offshore Mechanics and Arctic Engineering 129, 253–264. doi:10.1115/1.2199558.